

# Impurity levels and bandedge electronic structure in as-grown arsenic-doped HgCdTe by infrared photoreflectance spectroscopy

Jun Shao,\* Xiang Lü, Shaoling Guo, and Wei Lu

National Laboratory for Infrared Physics, Shanghai Institute of Technical Physics, Chinese Academy of Sciences, 200083 Shanghai, China

Lu Chen, Yanfeng Wei, Jianrong Yang, and Li He

Research Center for Advanced Materials and Devices, Shanghai Institute of Technical Physics, Chinese Academy of Sciences, 200083 Shanghai, China

Junhao Chu

National Laboratory for Infrared Physics, Shanghai Institute of Technical Physics, Chinese Academy of Sciences, 200083 Shanghai, China and Key Laboratory of Polar Materials and Devices, Ministry of Education, East China Normal University, 200062 Shanghai, China

(Received 8 April 2009; revised manuscript received 2 August 2009; published 16 October 2009)

The nature of bandedge electronic structure represents a theoretically interesting and technologically important question in arsenic-doped narrow-gap HgCdTe. In this study, temperature-dependent (11–290 K) photoreflectance (PR) measurements were carried out in midinfrared spectral region on three as-grown arsenic (As)-doped narrow-gap  $\text{Hg}_{1-x}\text{Cd}_x\text{Te}$  ( $x=0.317, 0.287, \text{ and } 0.310$ , respectively) samples prepared by molecular-beam epitaxy. Low-energy photomodulated Fabry-Pérot interference (FPI) and high-energy Franz-Keldysh oscillation (FKO) were analyzed and bandedge PR features were discriminated. Curve fittings of the bandedge PR features were performed, band-gap and below-gap PR processes were identified, and critical energies were determined. While no obvious FPI and FKO could be identified for the sample with a doping level of about  $10^{18} \text{ cm}^{-3}$ , they were strong for the doping levels of about  $10^{16}\text{--}10^{17} \text{ cm}^{-3}$ , and got enhanced with temperature. Detailed analyses indicated that the below-gap PR features are linked to donor-acceptor, conduction-band-acceptor, and donor-valence-band transitions. The average energy levels of the donor and acceptor states were evaluated to be about  $17 \pm 1 \text{ meV}$  and  $27 \pm 3 \text{ meV}$  below conduction-band minimum, and  $14 \pm 1 \text{ meV}$  above valence-band maximum at 77 K, and the origins were assigned to  $\text{As}_{\text{Hg}}$ ,  $\text{Te}_{\text{Hg}}$ , and  $\text{V}_{\text{Hg}}$ , respectively. The effect of possible deep-level impurities were also discussed, and a value of about 69 meV above the valence-band maximum was assumed preliminarily for the second level of  $\text{V}_{\text{Hg}}$  acceptor ( $\text{V}_{\text{Hg}}^{\text{II}}$ ) and 42 meV below the conduction-band minimum for As tetramer [ $(\text{As}_{\text{Hg}}\text{-As})_{\text{dimmer}}]_3$ . The evolution of PR critical energies with temperature was compared with an empirical formula for HgCdTe band-gap energy, and the implication of “effective band gap” was evidenced for the empirical formula. Finally, a schematic diagram was drawn for the bandedge electronic structure of the as-grown As-doped narrow-gap HgCdTe epilayers.

DOI: 10.1103/PhysRevB.80.155125

PACS number(s): 71.55.Gs, 78.66.Hf, 78.30.Fs, 78.20.Ci

## I. INTRODUCTION

$\text{Hg}_{1-x}\text{Cd}_x\text{Te}$  as a distinct narrow-gap semiconductor has attracted wide range of research interests in the last decades.<sup>1–6</sup> It is the material system of choice for high performance infrared detector arrays.<sup>7</sup> Meanwhile, it is also a good candidate for fundamental physics study.<sup>8–11</sup> By changing the composition  $x$ , the band-gap energy can cover a wide spectral range from near to far infrared. It is well known that the composition and temperature dependence of the band-gap energy can be represented by, e.g., Hansen *et al.*'s empirical formula,<sup>1</sup>

$$E_g(x, T) = -0.302 + 1.93x + 5.35(1 - 2x)T \times 10^{-4} - 0.810x^2 + 0.832x^3, \quad (1)$$

where  $E_g(x, T)$  is the band-gap energy,  $x$  is the Cd composition, and  $T$  is the sample's temperature. While the formula provides a rather fine approximation for material and device application, the physical meaning behind is less clear. Chu *et al.* suggested that the formula represents in the temperature range of 77–300 K the cutoff energy of photoconductive or

photovoltaic response curves.<sup>12</sup> The questions are therefore straightforward: what is the difference between the band-gap and cutoff energies and how is the cutoff energy affected by the factors other than the band gap?

Recently,  $p$ -type doping and impurity levels in the  $\text{Hg}_{1-x}\text{Cd}_x\text{Te}$  grown by molecular-beam epitaxy (MBE) technique have been a hot topic of consideration. Numerous exertions have been conducted from both the theoretical<sup>2,13,14</sup> and experimental<sup>4,15–17</sup> aspects. Theoretically, for example, *ab initio* calculations were carried out for the quantitative prediction of native point defect densities,<sup>2</sup> and density-functional theory was employed for analyzing the structural and electronic properties of arsenic (As) in HgCdTe.<sup>13,14</sup> The energy level of As as a single donor ( $\text{As}_{\text{Hg}}$ ) was suggested to be about 9 meV below the conduction-band minimum in  $\text{Hg}_{0.5}\text{Cd}_{0.5}\text{Te}$ .<sup>14</sup> Experimentally, the dependence of the Hall coefficient on temperature suggested that the ionization energy related to As as an acceptor ( $\text{As}_{\text{Te}}$ ) is less than 10 meV while the energy for mercury vacancy ( $\text{V}_{\text{Hg}}$ ) is about 85 meV for MBE-grown  $\text{Hg}_{0.72}\text{Cd}_{0.28}\text{Te}$  layers.<sup>15</sup> Meanwhile, a temperature-dependent absorption study indicated that the

TABLE I. Parameters for the as-grown As-doped  $\text{Hg}_{1-x}\text{Cd}_x\text{Te}$  epilayer samples prepared by molecular-beam epitaxy. The densities of As doping, electrons, and holes are in the unit of  $\text{cm}^{-3}$ , mobility in  $\text{cm}^2/\text{V}\cdot\text{s}$ .

Sample	$x$	$d$ ( $\mu\text{m}$ )	As density	77 K		300 K	
				hole density	mobility	electron density	mobility
as-1	0.317	8.3	$\leq 4 \times 10^{16}$	$7.4 \times 10^{15}$	153	$2.3 \times 10^{15}$	-5050
as-2	0.287	7.9	$6 \times 10^{18}$	$9.4 \times 10^{15}$	468	$2.9 \times 10^{15}$	-3810
as-3	0.310	9.8	$3 \times 10^{17}$	$6.1 \times 10^{16}$	520	$1.5 \times 10^{15}$	-6260

energy level of  $V_{\text{Hg}}$  as an acceptor is about 9–12 meV above the valence-band maximum of  $\text{HgCdTe}$ .<sup>18</sup> This value was recently proved to be reasonable by an optical study of  $\text{HgCdTe}$  photodiode structures.<sup>19</sup> The problems remain, however, that there were obvious contradictions in the reported values of the impurity levels, and the second level of  $V_{\text{Hg}}$  was not experimentally observed even though mercury vacancy was theoretically predicted to be a double-level acceptor.<sup>2</sup>

Photoreflectance (PR) as a powerful modulation spectroscopy has been widely employed in characterizing semiconductor electronic band structures in the short-wavelength ( $\leq 4 \mu\text{m}$ ) spectral region.<sup>20–26</sup> Its derivative nature suppresses uninteresting background effects and emphasizes structures located in the energy range of interband transitions and other weak features that may not be detected in conventional optical reflectance spectra.<sup>27,28</sup> Recently, a step-scan Fourier transform infrared (FTIR) spectrometer-based PR technique was developed,<sup>29,30</sup> which warranted the application in the midinfrared,<sup>31,32</sup> and manifested the feasibility in the far infrared<sup>33</sup> of up to 20  $\mu\text{m}$ . Preliminary results indicated that the bandedge PR line shape is relevant to shallow impurities and evolves with temperature in narrow-gap  $\text{HgCdTe}$ . By analyzing the temperature dependence of the PR line shape, near-bandedge processes were resolvable and the positions of shallow impurity levels were inferable.<sup>32</sup> To quantitatively clarify the near bandedge electronic structure and shallow levels, however, any oscillatory behavior has to be first discriminated from the real bandedge related PR features.

In this work, temperature-dependent (11–290 K) PR study is performed on three as-grown As-doped narrow-gap  $\text{Hg}_{1-x}\text{Cd}_x\text{Te}$  ( $x=0.317$ , 0.287, and 0.310) epilayer samples by the step-scan FTIR spectrometer-based PR technique.<sup>29</sup> The evolution of PR features with temperature are evidenced near the band gap with aid of Fabry-Pérot interference (FPI) and Franz-Keldysh oscillation (FKO) analyses. The mechanisms of particular PR features are discussed, and the average energy levels of the impurities  $\text{As}_{\text{Hg}}$ ,  $\text{Te}_{\text{Hg}}$ , and  $V_{\text{Hg}}$  are estimated to be about  $17 \pm 1$  meV and  $27 \pm 3$  meV below the conduction-band minimum and  $14 \pm 1$  meV above the valence-band maximum, respectively. A schematic diagram is suggested for the band gap and the near band-gap shallow impurity levels in as-grown As-doped narrow-gap  $\text{HgCdTe}$ . Comparison of the temperature-dependent energies of the PR features is made with Hansen *et al.*'s empirical formula and the physical implication of the “effective” band-gap energy is clarified for the empirical formula.

The paper is organized as follows. In Sec. II, brief introduction is made on the experimental details of sample preparation and PR measurement, as well as on the theoretical background about PR line-shape, FPI, and FKO analyses. In Sec. III, after the discrimination of bandedge PR features from the FPI and FKO in Sec. III A, line-shape analyses of the bandedge-related PR features are carried out and the evolution of critical point energy with temperature is clarified in Sec. III B, on which impurity levels are estimated, bandedge electronic structure is schematically drawn, and the nature of “effective” band-gap energy is suggested for Hansen *et al.*'s empirical formula. Finally in Sec. IV, a summary is made.

## II. EXPERIMENT

Three as-grown As-doped  $\text{Hg}_{1-x}\text{Cd}_x\text{Te}$  samples were used in this study, which were grown in a Riber 32P MBE system on undoped semi-insulating GaAs (211)B substrate at a temperature around 183 °C.<sup>34</sup> A 3- $\mu\text{m}$ -thick CdTe buffer layer was grown prior to  $\text{HgCdTe}$  nucleation. A pure As source was employed for the doping. The Cd composition  $x$  was determined by taking the energy corresponding to the  $500 \text{ cm}^{-1}$  absorption-coefficient point on transmission spectrum as the band-gap energy and compared to the empirical formula Eq. (1). The samples were  $p$  type at 77 K due to high density of  $V_{\text{Hg}}$ . At room temperature, however, the samples were  $n$  type due to the thermal excitation and As atoms resided predominantly on cation side ( $\text{As}_{\text{Hg}}$ ) as donors.<sup>35,36</sup> The samples are denoted by as-1, as-2, and as-3, respectively, their parameters are summarized in Table I for composition, thickness, doping level, and carrier density and mobility.

The step-scan FTIR spectrometer-based PR technique is used in this study,<sup>30</sup> which enhances spectral resolution and signal-to-noise ratio significantly even in the mid- and far-infrared spectral regions, reduces time consumption, and may hence warrant a systematic temperature-dependent measurement. A step-scan FTIR spectrometer (Bruker IFS 66 v/S) is configured with KBr beamsplitter and liquid-nitrogen cooled photovoltaic  $\text{HgCdTe}$  detector for a sensitive spectral range of about 0.11–0.6 eV. A Globar wideband source is used for probing light and an  $\text{Ar}^+$  laser (Spectra-Physics BeamLok 2065) set to the 514.5 nm line is employed for pumping light. The samples are mounted on the cold finger of a cycling cryodrive to keep at a particular temperature in the range of 11–290 K. For comparison, conventional reflectance spectra are recorded at about room temperature with an identical angle of reflection.

It is textbook knowledge that a PR spectrum can be fitted by a line shape function for unbound situation and low electrical field modulation,<sup>20,29,37</sup>

$$\frac{\Delta R}{R} = \text{Re} \sum_{i=1}^k A_i e^{j\phi_i} (E - E_i + j\Gamma_i)^{-m}, \quad (2)$$

where  $k$  is the total number of PR features,  $A_i$  and  $\phi_i$  are the amplitude and phase of the  $i$ th PR feature, and  $\Gamma_i$  are the energy and broadening parameter of the particular transition,  $m=2.5$  for a three-dimensional critical point.<sup>20</sup> Based on such a fitting procedure, the critical energy of each PR feature,  $E_i$ , can be derived.

When an intermediate electric field occurs in the material, FKO may emerge. The oscillatory behavior at  $E > E_g$  can be described by an electro-optic function, whose extreme are represented by<sup>38</sup>

$$l\pi = \phi + \frac{4}{3} \left( \frac{E_l - E_g}{\hbar\theta} \right)^{3/2}, \quad (3)$$

where  $\hbar\theta = (e^2 \hbar^2 F^2 / 2\mu_{\parallel})^{1/3}$ ,  $l$  is the extreme index,  $\phi = \pi(m-1)/4$  with  $m$  is dimensionality of the critical point and takes a value of 2.5 in this case,  $E_l$  is the energy of the  $l$ th oscillation extreme,  $F$  is the electric field, and  $\mu_{\parallel}$  is the reduced interband effective mass in the direction of the electric field  $F$ . A plot of  $E_l$  versus  $[(3\pi/4)(l-3/8)]^{2/3}$  is therefore a straight line, with its slope to be proportional to  $F$  and interception to be  $E_g$ .<sup>39,40</sup>

Oscillatory behavior of the line shape was also observed in the PR spectra at  $E < E_g$  of GaAs,<sup>41</sup> of which the modulation of the refractive index in heavily doped samples was assumed as a main reason. The possible mechanism of either (i) band filling of impurity states or (ii) electric field or FK effect was, however, not yet clear.<sup>41</sup>

By measuring the wavelengths of two adjacent minima in a conventional reflectance spectrum just below the band gap, it is deducible that<sup>42</sup>

$$2n \left( \frac{d}{\cos \phi} \right) = \left( \frac{1}{\lambda_2} - \frac{1}{\lambda_1} \right)^{-1} = \frac{1}{\Delta\nu}, \quad (4)$$

where  $\phi$  is the angle of reflection in the layer,  $n$  is the refractive index, and  $d$  is the thickness of the layer. Though it is valid only if  $n$  is independent of  $\lambda$  over the range, it can provide a qualitative understanding of the FPI pattern in conventional reflectance measurement.

### III. RESULTS AND DISCUSSION

#### A. Discrimination of bandedge PR features from oscillations

Typical PR spectra are illustrated in Fig. 1 for the three  $\text{Hg}_{1-x}\text{Cd}_x\text{Te}$  samples at 77 and 200 K, respectively. PR features with dominant intensity are clearly seen in the energy region of about 0.23 eV at 77 K and 0.28 eV at 200 K. They differ from sample to sample with different composition and doping level, and evolve in line shape and move to higher energy as temperature rises. The central energy of the dominant PR features is very close to that predicted by Eq. (1) for the band-gap energy of  $\text{Hg}_{1-x}\text{Cd}_x\text{Te}$ . The bandedge related

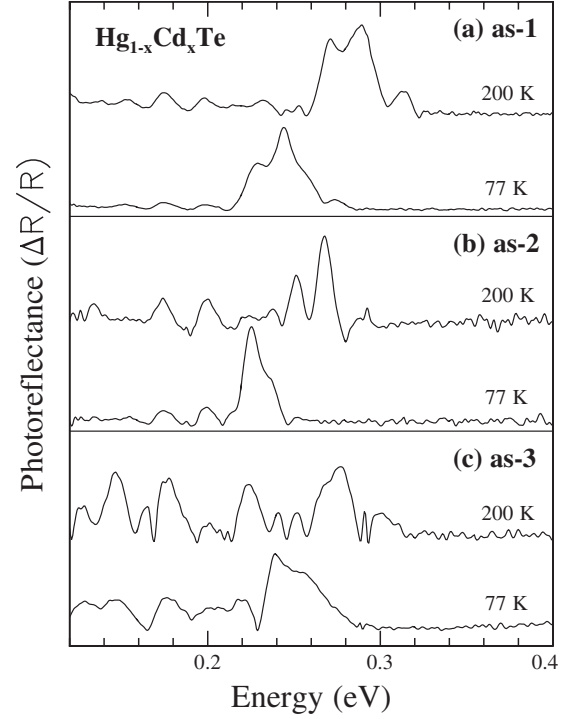


FIG. 1. PR spectra recorded at 77 and 200 K, respectively, for the  $\text{Hg}_{1-x}\text{Cd}_x\text{Te}$  samples of (a) as-1 with  $x=0.317$ , (b) as-2 with  $x=0.287$ , and (c) as-3 with  $x=0.310$ .

nature of these dominant PR features is also approved by comparing them to corresponding PL spectra taken at nominally identical temperatures.<sup>32</sup> Moreover, several weaker PR features can be identified in the energy range below the dominant PR features, especially for the as-2 and as-3 samples and at 200 K. Due to the nature of high concentration impurities of the samples, deep-level impurity and below band-gap interference effect<sup>41</sup> are both the possible origins.

It is therefore necessary to first distinguish the impurity- and band-related PR features from any FKO above the band gap or back-surface reflectance effect<sup>43</sup> below the band gap, before the investigation of impurity levels and bandedge electronic structures. On one hand, any “fake” levels can be avoided so as to establish a reliable picture of bandedge electronic structure, and on the other hand, the “real” energy levels can be traced out correctly and determined quantitatively so as to obtain accurate information about the band gap and impurities.

Figure 2 shows a series of infrared PR spectra recorded at different temperatures in the range of 11–290 K for the as-1  $\text{Hg}_{0.683}\text{Cd}_{0.317}\text{Te}$  sample. Generally, the PR line shape is rather complex, especially at high temperatures. While only a set of broad and relatively strong PR features is clearly seen at extremely low temperatures, which will be noted as “main PR features” hereafter, two sets of distinct features on the low- and high-energy sides of the main PR features can be identified at high temperatures.

The main PR features evolve with temperature in two manners: (i) the intensity is dominated in turn by low-energy PR feature(s) at low temperature and by high-energy one(s)

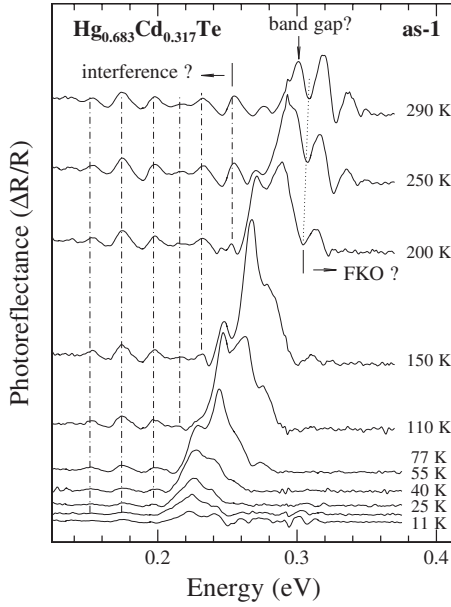


FIG. 2. PR spectra for as-1 sample in temperature range of 11–290 K. Vertical dashed dots mark maxima in “interference ?” region. Extrema on the right side of dotted line are denoted by “FKO ?.” Possible band gap is marked by vertical arrow on the spectrum at 290 K.

as temperature rises, and (ii) each of the individual main PR features moves to higher energy with temperature in a similar trend as the HgCdTe band-gap energy. Such phenomena have been recently shown to be due to photomodulation of impurity-band and band-band reflectance, their intensities correlate to the joint concentration of the involved energetic states.<sup>32</sup>

The low-energy set, which is denoted by “interference ?” in Fig. 2, shows up already at moderate temperature with periodic oscillatory extrema, and gets more obvious as temperature rises. The energetic positions of the extrema, however, do not change obviously as indicated by the vertical dashed dots in Fig. 2. When temperature rises up to near room temperature, the high-energy set of PR features marked by “FKO?” emerges and manifests obvious oscillatory behavior. The corresponding extrema seem to be unchanged in energy with temperature. It is worthy to emphasize that the temperature-dependent behavior of the low- and high-energy sets are in clear contrast to the main PR features.

The high-energy set of oscillatory PR features is ascribed to FKO based on the following matters of facts. First, as depicted in Fig. 3, the extreme energy  $E_l$  as a function of  $[(3\pi/4)(l-3/8)]^{2/3}$  can be least-square fitted by a straight line quite well. The slope is  $(9.0 \pm 0.5) \times 10^{-3}$ ,  $(10.0 \pm 0.3) \times 10^{-3}$ , and  $(9.9 \pm 0.3) \times 10^{-3}$  eV, and the interception  $E_g$  is  $0.292 \pm 0.001$ ,  $0.294 \pm 0.001$ , and  $0.295 \pm 0.001$  eV for the temperatures of 200, 250, and 290 K, respectively. This is a direct evidence for the nature of FKO. An electric field  $F$  of about 4.4–5.0 kV/cm is deduced and an equivalent surface charge density of  $\sim 10^{10}$  cm<sup>-2</sup> is estimated, with an assumption of reduced interband effective mass  $\mu_{||} \approx 0.01m_0$ . Second, although the sample is *p* type at 77 K, it evolves to *n* type as temperature exceeds about 180 K and hence there are

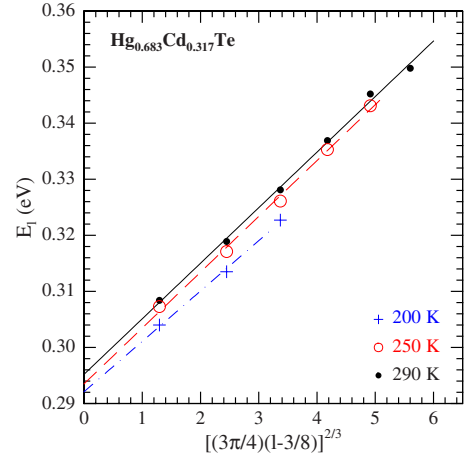


FIG. 3. (Color online) Extreme energy  $E_l$  as a function of  $[(3\pi/4)(l-3/8)]^{2/3}$  for the high-energy PR features of the as-1 sample at 200, 250, and 290 K, respectively. +, ○, and ● are experimental data, dashed dot, dashes, and solid line are least-square fits.

free carriers with higher mobility. Lastly, the extreme energies depicted in Fig. 3 do not change with temperature obviously, in clear contrast to the temperature dependence of the band-gap energy described by Eq. (1). Meanwhile, the extreme energies are higher than the band-gap energy suggested by Eq. (1) even at 290 K and for the lowest extreme index. It will be illustrated shortly afterwards in Fig. 10 that the empirical formula provides a reasonable description of the band-gap energy at about room temperature in a similar case for the as-2 sample. This excludes the possibility of assuming any of the high-energy oscillatory PR features to be corresponding directly to the band gap.

To identify the origin of the low-energy oscillatory features, conventional reflectance measurement is performed at room temperature in a similar configuration of optics with a nominally identical angle of reflection. The spectrum is plotted in Fig. 4, together with the PR spectrum recorded at 290 K.

Two distinct features are obvious that (i) the maxima of the oscillations in the PR spectrum correspond exactly to the oscillatory minima in the conventional reflectance spectrum as indicated by the dashed dots in Fig. 4, and (ii) the energy separation between two adjacent maxima is about 20 meV, which corresponds closely to the FPI caused by the top- and bottom-surface/interface of the Hg<sub>0.683</sub>Cd<sub>0.317</sub>Te layer. These indicate that the low-energy oscillations in the PR spectra are due to a particular type of FPI introduced by the reflection at the top air/HgCdTe interface and the photomodulated reflection at the bottom HgCdTe/CdTe interface. The mechanism behind may be as follows. On one hand, because of the photomodulation of refractive index of HgCdTe, the interference changes with the same frequency as the pumping laser being chopped and hence can be traced out together with the main PR features near the band gap. On the other hand, as the photomodulation of refractive index  $\Delta n$  is related to modulated reflectance  $\Delta R$ ,<sup>41</sup>

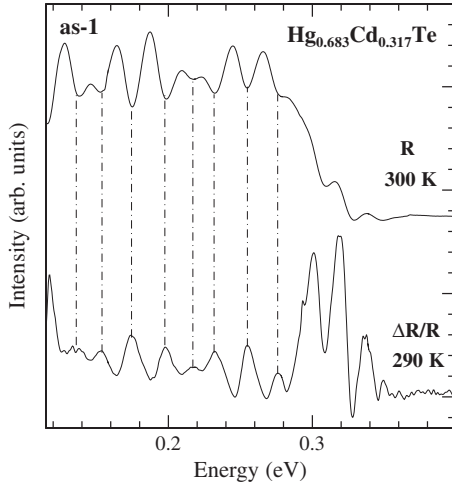


FIG. 4. Comparison of conventional reflectance ( $r$ ) at room temperature and PR ( $\Delta R/R$ ) at 290 K for as-1 sample. Vertical dashed dots indicate oscillatory minima of  $R$  spectrum.

$$\Delta n = [(n+1)^3/4(n-1)]\Delta R, \quad (5)$$

the change to the refractive index  $n$  is very small ( $\leq 10^{-3}$ ), and hence the periodic behavior of the oscillations in the PR spectrum is very close to that in the conventional reflectance spectrum.

Figure 5 depicts a series of infrared PR spectra for the as-2 sample at different temperatures in the range of 11–290 K, giving special attention to the low- and high-energy sides of the main PR features marked by vertical dashed dots. In a previous study,<sup>32</sup> the evolution of the main PR features with temperature was well identified for this sample, and the bandedge related nature was clarified. Falling short of certain judgment on the low- and high-energy PR features, however,

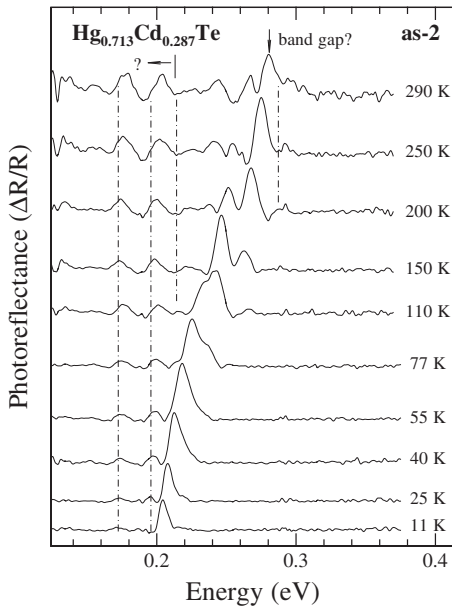


FIG. 5. PR spectra for as-2 sample in temperature range of 11–290 K. Vertical dashed dots in “?” region mark the maxima of PR features at low temperature.

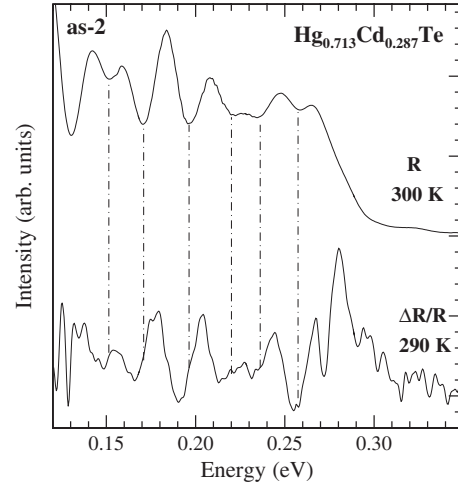


FIG. 6. Comparison of conventional reflectance ( $r$ ) at room temperature and PR ( $\Delta R/R$ ) at 290 K for as-2 sample. Vertical dashed dots mark oscillatory minima of  $R$  spectrum.

neither proper curve fitting of the whole PR spectrum nor quantitative analysis of critical point energies of the low-energy features could be made at that time.<sup>32</sup> It is clearly seen in Fig. 5 that while the main PR features evolve with temperature in a similar manner as those of the as-1 sample, the situation is rather different in two aspects. First, no obvious FKO can be assumed even at about room temperature on the high-energy side of the main PR features, in contrast to the as-1 sample. Second, although the weak PR features marked by “?” are detectable on the low-energy side of the main PR features even at low temperature and gain their intensity as temperature rises, their maxima show clear blue shift with temperature, which is again in obvious contrast to the as-1 sample.

To check further if the low-energy weak PR features are, as those of the as-1 sample, due to photomodulated FPI, similar comparison is made between the PR spectrum at 290 K and a conventional reflectance spectrum at room temperature. The result is illustrated in Fig. 6, in which the vertical dashed dots mark the energetic positions of the FPI minima of the conventional reflectance spectrum. Not as the as-1 sample, here the minima of the conventional reflectance do correspond to neither the maxima nor the minima of the low-energy weak PR features. Furthermore, the average energy separation between two adjacent maxima of the low-energy PR features is about 23 meV, which deviates from the average value of about 21 meV between two adjacent minima of the conventional reflectance. As indicated by Eq. (5), photomodulated refractive index  $\Delta n$  is very small. It is therefore conclusive that the low-energy PR features are unlikely to be FPI, but may be introduced by deep-level related process.

It was known that<sup>38</sup> FKO was easily observed in III-V semiconductor samples with a doping level of about  $10^{16} \text{ cm}^{-3}$ . Higher doping level increases the concentration of dopant impurity and introduces more defects, which will reduce carrier mobility and may depress the FKO strength. As listed in Table I, the as-1 sample has a doping level of about  $4 \times 10^{16} \text{ cm}^{-3}$ , and an electron density of 2.3

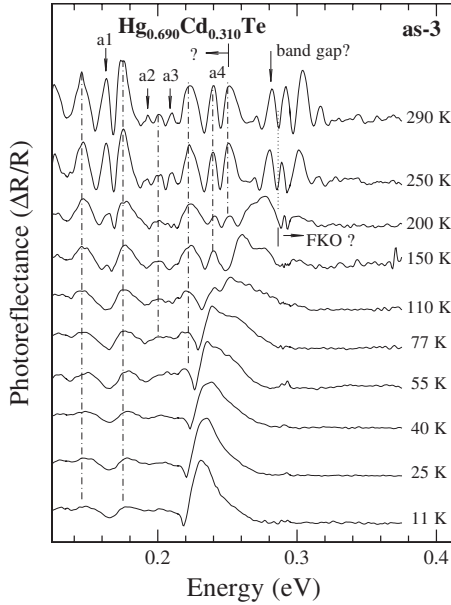


FIG. 7. PR spectra for as-3 sample in temperature range of 11–290 K. Vertical dashed dots in “?” region mark the maxima of PR features at low temperatures.

$\times 10^{15} \text{ cm}^{-3}$  and a mobility of  $-5050$  at room temperature. Meanwhile, the as-2 sample has a doping level of  $6 \times 10^{18} \text{ cm}^{-3}$ , and an electron density of  $2.9 \times 10^{15} \text{ cm}^{-3}$  at room temperature, its carrier mobility at room temperature, however, is obviously lower than that of the as-1 sample. These depress the FKO, and provide a good chance for the doping related impurities being evidenced in PR spectra.

Such a doping-level effect can be verified by similar analysis of the as-3 sample with a intermediate doping level of  $3 \times 10^{17} \text{ cm}^{-3}$ . In Fig. 7, a series of infrared PR spectra is depicted for the sample at different temperatures in the range of 11–290 K. The main PR feature dominating the PR spectra at low temperatures manifests blue shift as temperature rises, its line shape evolves in the similar manner as the as-1 and as-2 samples behave. The low-energy PR features, on the other hand, get enhanced with temperature while the maxima do not shift as marked by vertical dashed dots in Fig. 7, which is very similar to the as-1 sample. It is distinct, however, that new maxima of a1-a4 emerge in the low-energy region marked by “?” soon as temperature rises up to 150 K, and get stronger as temperature goes up further. In the meantime, new PR features denoted by “FKO?” show up as the FKO of the as-1 sample in the high-energy region.

To root out the possible origin of the low-energy PR features, a comparison of conventional reflectance spectrum with PR spectrum at a nominally identical temperature of 290 K is invoked, as illustrated in Fig. 8. It is obvious that the maxima of the PR spectrum are energetically coincident with the minima of the conventional reflectance spectrum as marked by vertical dashed dots, except for the additional a1-a4 PR features emerging at about 0.164, 0.193, 0.210, and 0.239 eV, respectively, for the temperatures not lower than 150 K. This leads to a conclusion that the low-energy PR features already detectable at low temperature are due mainly to FPI. Meanwhile, the additional a1-a4 PR features may be

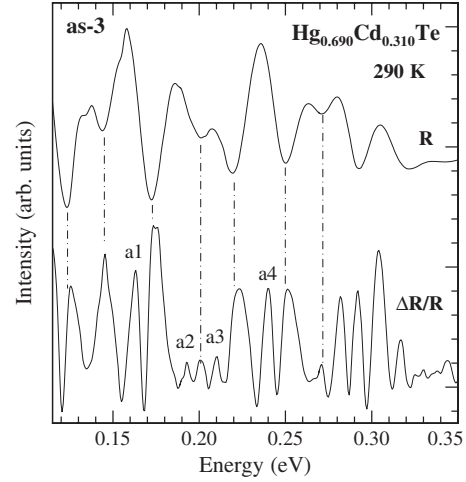


FIG. 8. Comparison of conventional reflectance ( $r$ ) and PR ( $\Delta R/R$ ) at 290 K for as-3 sample. Vertical dash-dots mark oscillatory minima of  $R$  spectrum.

ascribed preliminarily to be impurity-level related by taking into account the evolution of deep-level related PR features observed for the as-2 sample. Further evidence will be established by energy analysis in Sec. III B.

Analysis of the high-energy PR features in a similar manner as for the as-1 sample suggests the FKO nature, with an electric field of about 3.3 kV/cm and band-gap energy of about 0.274 eV at 290 K. It is worthy to emphasize that the scale down of the field relative to that of the as-1 sample at a nominally identical temperature is in good agreement with the relation of electron densities for the two samples at room temperature, and can therefore be taken as a support for the FKO ascription.

As a short summary, FPI and FKO coexist on the both sides of the main PR features in the as-1 and as-3 samples with relatively low doping levels of about  $4 \times 10^{16} \text{ cm}^{-3}$  and  $3 \times 10^{17} \text{ cm}^{-3}$ , respectively. The FPI is so strong that no deep-level related PR feature can be assumed reliably in the spectral range where the FPI shows up, especially at low temperatures. The situation is rather different for the as-2 sample with a considerably high doping level of about  $6 \times 10^{18} \text{ cm}^{-3}$  that neither FPI nor FKO is significant relative to the corresponding main PR features. Meanwhile, high doping level makes deep-level related PR features to be detectable, and hence may serve as a pathway for optical characterization of deep-level impurities/defects. It is noteworthy that the FPI referenced here is very likely the back-surface reflectance effect previously observed in III-V semiconductors.<sup>43</sup> The mechanism behind may be the photo-modulation of refractive index.

### B. Impurity levels and bandedge electronic structure in as-grown arsenic-doped HgCdTe

Having discriminated the bandedge related PR features from FPI and FKO for the as-1 and as-3 samples, and confirmed the PR features of the as-2 sample to be related solely to the bandedge electronic structure, it is right time to carry out line shape analyses so as to clarify impurity levels and

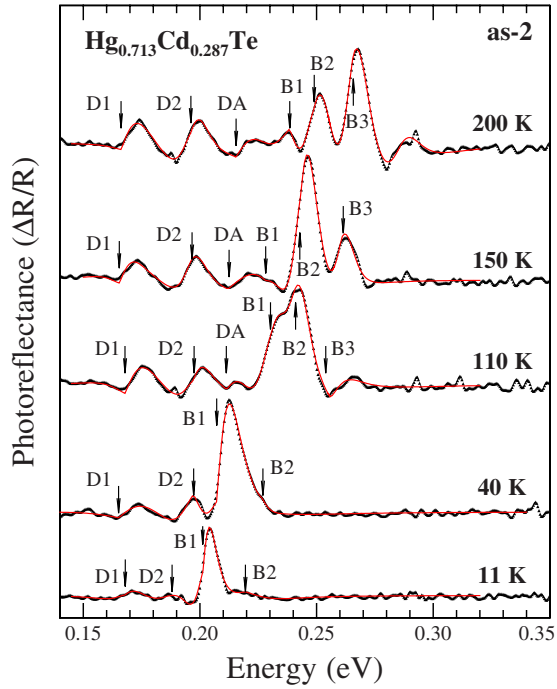


FIG. 9. (Color online) PR spectra (in dots) and curve fittings (in solid lines) for as-2 sample at 11, 40, 110, 150, and 200 K, respectively. Critical points are marked by arrows and labels of D1, D2, DA, B1, B2, and B3.

bandedge electronic structure in as-grown As-doped HgCdTe epilayers.

Figure 9 illustrates the PR spectra in dots for the as-2 sample at several representative temperatures. Curve fitting procedures are performed based on Eq. (2), and the results are directly overlaid as solid lines on the experimental spectra. The critical points determined are marked by vertical arrows and the labels. It is worthy to emphasize here that not only the main PR features of B1, B2, and B3, but also the low-energy features of D1, D2, and DA are well reproduced by the curve fittings, owing to the certain judgment of the impurity-related nature of the low-energy PR features. This is in obvious contrast to the previous study,<sup>32</sup> where only the intensity evolution of the main PR features with temperature were clarified because the PR spectrum as a whole could not be fitted reliably without necessary information on the low-energy PR features.

The main PR features B1, B2, and B3 show clear evolution of intensity with temperature, in the same manner as already clarified in the previous study.<sup>32</sup> Due to the fact that the DA feature is rather weak and the D1 and D2 features are well separated, fitting the main PR features alone or as a part of the whole PR spectrum does not produce obvious difference to the intensities and critical energies of the B1-B3 features. Therefore, the results of the previous theoretical simulation keep valid that B1 originates from photomodulation-induced screening of donor-acceptor pairs, and B2 is due to photomodulation of built-in electric field, which causes acceptor-conduction-band and valence-band-donor reflectance to be modulated, similar to the B3 band-band process. The related donor and acceptor levels were

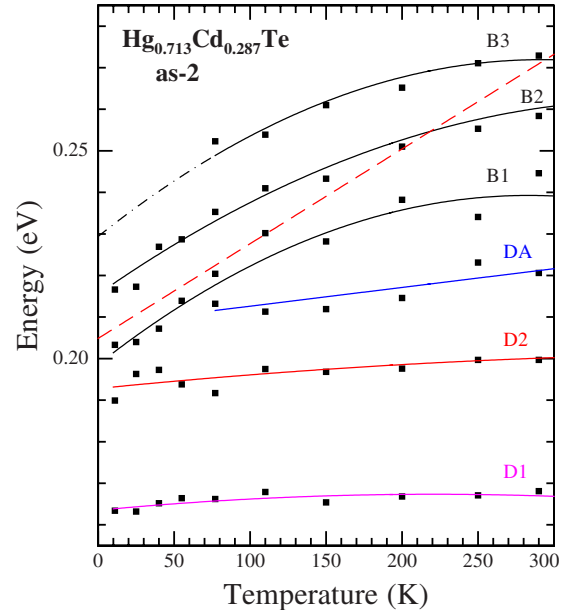


FIG. 10. (Color online) Evolution of critical point energy with temperature for B3, B2, B1, DA, D2, and D1 PR features of as-2 sample. Dashed line is according to Hansen *et al.*'s empirical formula [Eq. (1)], solid lines represent least-square fittings of individual sets of data points.

deduced as  $\sim 18$  meV below the conduction band and  $\sim 14$  meV above the valence band.<sup>32</sup>

For the low-energy weak PR features D1, D2, and DA, on the other hand, the intensity evolution is not so obvious. The general trend is a very slight enhancement of intensity with temperature for the D1 and D2 features. This may hint a deep-level nature of the impurity levels related to the D1 and D2 PR features.

The critical point energies determined by the line shape fittings of the whole PR features are depicted against temperature in Fig. 10 for the as-2 sample. Least-square fitting is made for the temperature-dependent energy of each PR feature, and is overlaid as a solid line directly on the experimental data. For a direct comparison, a calculation of the band-gap energy as a function of temperature is made using Eq. (1), and the result is depicted in Fig. 10 as dashes.

Clearly, the energies of the main PR features B3, B2, and B1 manifest strong temperature dependence. From the plot, the energetic separation between the B3 and B2 PR features is estimated to be about 16 meV, and that between the B3 and B1 features is about 32 meV. These two values are exactly the average and the summation of 18 and 14 meV, respectively, and are consistent with the aforementioned values deduced from the theoretical simulation of the intensity evolution.<sup>32</sup> It therefore provides a solid support for the discussion of the mechanisms of the main PR features. Meanwhile, the temperature dependence of the transition energy is rather weak for the DA feature. As a result, the separation between the B3 and DA features increases with temperature. It takes a value of about 40 meV at 77 K, and a rather big value of about 47 meV when temperature rises to 150 K. The energies of D1 and D2 do not show obvious dependence on temperature, manifesting the characteristic of deep levels. At

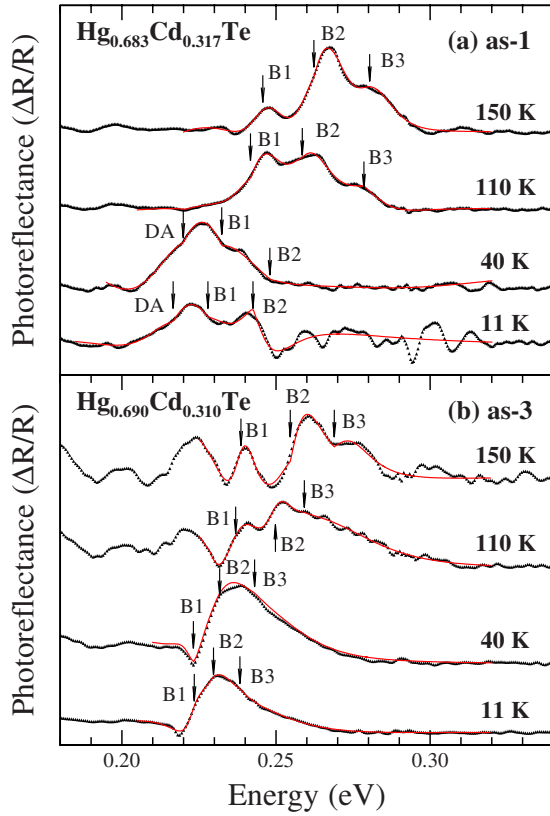


FIG. 11. (Color online) PR spectra (in dots) and curve fittings (in solid lines) of the main PR features for as-1 (a) and as-3 (b) samples at 11, 40, 110, and 150 K, respectively. Critical points are marked by arrows and labels DA, B1, B2, and B3.

77 K, the separations are approximately 84 meV for the B3 and D1, and 53 meV for the B3 and D2 features, respectively.

Similar curve fitting procedures are also performed on the main PR features of the as-1 and as-3 samples in a temperature range of up to 150 K, as illustrated in Fig. 11(a) and 11(b), respectively. The experimental PR spectra are plotted in dots, and the fitted curves of the main PR features are directly overlaid as solid lines. The critical points are marked by vertical arrows, and are ascribed to DA, B1, B2, and B3, respectively, based on the evolution of the PR line shape in a wide temperature range of 11–290 K. It is clear that the main PR feature’s energy and intensity evolve with temperature in a similar manner as the as-2 sample. Due to the obvious FKO, however, the analyses at higher temperatures are hold back. Meanwhile, the analyses of weak D1 and D2 PR features for the as-1 sample and D1, D2 and DA for the as-3 samples are impossible because of the strong FPI even at low temperatures.

The critical point energies determined by the line shape fittings are depicted against temperature in Fig. 12. Least-square fitting is made for the temperature-dependent energy of each PR features, and is overlaid as solid line directly on the data points. From Fig. 12(a), the energetic separations between the B3 and B2, B3 and B1, and B3 and DA are estimated to be about 17, 33, and 46 meV, respectively, for the as-1 sample at 77 K. For the as-3 sample at 77 K as

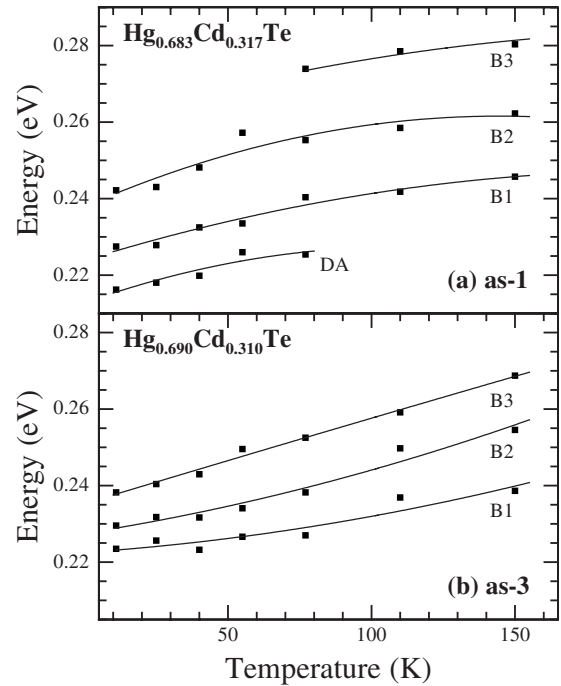


FIG. 12. Evolution of critical point energy with temperature for B3, B2, B1, and DA PR features of as-1 (a) and as-3 (b) samples. Solid lines represent least-square fittings of individual sets of data points.

indicated in Fig. 12(b), the energetic separations between the B3 and B2, and B3 and B1 are about 15 and 28 meV, respectively. These values are very close to those of the as-2 sample, indicating the same characteristic of the main PR features. It is worthy to indicate that the band-gap energy at 150 K is as suggested in Fig. 12 about 0.282 and 0.268 eV for the as-1 and as-3 samples, respectively. According to the temperature dependence of the B3 energy for the as-2 sample as illustrated in Fig. 10, the band-gap energy can be estimated to be 0.287, 0.291, and 0.292 eV for the as-1 sample at 200, 250, and 290 K, and 0.278 eV for the as-3 sample at 290 K, respectively. These values are in good agreement with those determined by the aforementioned FKO analyses, and can hence serve as solid evidence for the assignment of band-band nature to the B3 PR feature, as well as for the ascription of FKO to the oscillatory behavior in the energy range above the main PR features. Meanwhile, the B3 energy of the as-3 sample at 77 K is about 0.252 eV. As aforementioned, the additional PR features a1-a4 emerge in the low-energy side of the main PR features at high temperatures at about 0.164, 0.193, 0.210, and 0.239 eV, the separations between the B3 and a1-a4 are correspondingly 88, 59, 42, and 13 meV. These values are very close to those of the as-2 sample between the B3 and D1, B3 and D2, B3 and DA, and B3 and B1 at 77 K, respectively. It is therefore conclusive that the a1-a3 additional PR features identified for the as-3 sample at high temperatures are impurity-level related, and have the same origin as the D1, D2, and DA of the as-2 sample.

To determine to which impurity levels the individual PR features being related, the following matters of facts must be

taken into account. First, the samples are  $p$  type at 77 K with relatively low carrier mobility of an order of  $10^2$ , and become  $n$  type at room temperature with the mobility being enhanced by a factor of about 10. Second, it was predicted by first-principles calculations that the tellurium antisite ( $\text{Te}_{\text{Hg}}$ ), besides the double acceptor  $\text{V}_{\text{Hg}}$ , is an important native point defect, and may be a donor located energetically about 25 meV below the conduction-band minimum for  $\text{Hg}_{0.8}\text{Cd}_{0.2}\text{Te}$ .<sup>2</sup> It is believed to be the defect responsible for the  $n$ -type carrier concentrations in as-grown  $\text{HgCdTe}$  prepared by MBE technique. A recent demonstration of far-infrared PR measurement indicated that the PR features can be well clarified for a  $p$ -type annealed As-doped  $\text{Hg}_{0.77}\text{Cd}_{0.23}\text{Te}$  if a shallow level of  $26.4 \pm 0.5$  meV below the conduction band is assumed for  $\text{Te}_{\text{Hg}}$ .<sup>33</sup> Furthermore, as suggested by *ab initio* calculations for the *in situ* As-doped  $\text{HgCdTe}$ , the arsenic atoms reside predominantly on the cation sublattice ( $\text{As}_{\text{Hg}}$ ) at 185 °C under tellurium-saturated conditions during MBE growth, and a large fraction of them are bound to cation vacancies forming  $\text{As}_{\text{Hg}}\text{-V}_{\text{Hg}}$  complex.<sup>13</sup>

It is hence reasonable to ascertain that the B3 feature is originated in conduction-band-valence-band process, while the B2 feature is contributed by conduction band- $\text{V}_{\text{Hg}}$  and  $\text{As}_{\text{Hg}}$ -valence band joint concentrations, and the B1 is due to  $\text{As}_{\text{Hg}}\text{-V}_{\text{Hg}}$  complex at extremely low temperatures and  $\text{As}_{\text{Hg}}$  donor- $\text{V}_{\text{Hg}}$  acceptor joint concentration at higher temperatures. The energy levels of  $\text{As}_{\text{Hg}}$  and  $\text{V}_{\text{Hg}}$  are approximately  $17 \pm 1$  meV below the conduction-band minimum and  $14 \pm 1$  meV above the valence-band maximum, respectively, and the  $\text{As}_{\text{Hg}}\text{-V}_{\text{Hg}}$  complex has a small binding energy of about 1.2 meV for the as-2 sample at extremely low temperatures.<sup>32</sup> The DA feature may be related to  $\text{Te}_{\text{Hg}}$  donor- $\text{V}_{\text{Hg}}$  acceptor joint concentration and  $\text{Te}_{\text{Hg}}$  level locates at about  $27 \pm 3$  meV below the conduction-band minimum.

With these energy levels, information can be drawn from the evolution of the main PR features with temperature that (i) a rather big fraction of the As is bounded to  $\text{V}_{\text{Hg}}$  and forms  $\text{As}_{\text{Hg}}\text{-V}_{\text{Hg}}$  complex at low temperature, (ii) the concentration of the isolated  $\text{V}_{\text{Hg}}$  is similar to or even slightly higher than that of the isolated  $\text{As}_{\text{Hg}}$ . These are in good agreement with a theoretical prediction of impurity and defect concentration for  $\text{Hg}_{0.7}\text{Cd}_{0.3}\text{Te}$  equilibrated at 175 °C under tellurium-saturated conditions,<sup>44</sup> and the energy for  $\text{V}_{\text{Hg}}$  acceptor level is very close to that derived from temperature-dependent absorption study of undoped  $\text{HgCdTe}$ .<sup>18</sup>

The average energy separation is about 86 meV between the B3 and D1 (a1) features at 77 K, which is nearly the same as that suggested for  $\text{V}_{\text{Hg}}$  acceptor level, 85 meV, by Hall measurement.<sup>15</sup> As both the D2 (a2) and D1 (a1) features are observed only in the samples with relatively high As-doping levels, the intensity evolution of the D2 feature with temperature is similar to that of the B1 feature, and  $\text{V}_{\text{Hg}}$  is known to be a double-level acceptor, we may suppose that (i) the D1 feature is related to the  $\text{As}_{\text{Hg}}$  donor and the second acceptor level of  $\text{V}_{\text{Hg}}$  ( $\text{V}_{\text{Hg}}^{\text{II}}$ ), and hence the  $\text{V}_{\text{Hg}}^{\text{II}}$  level is about 69 meV above the valence-band maximum at 77 K, while (ii) the D2 feature is introduced by high concentration As dopant, which results in considerable concentration of complex defects of  $[(\text{As}_{\text{Hg}}\text{-As}_i)_{\text{dimmer}}]_3\text{-V}_{\text{Hg}}$ .<sup>45</sup>

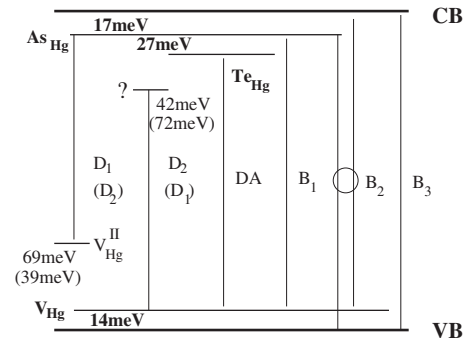


FIG. 13. Schematic of bandedge electronic structure and related PR processes in as-grown As-doped  $\text{Hg}_{1-x}\text{Cd}_x\text{Te}$  epilayers prepared by MBE technique. CB and VB represent conduction- and valence-band,  $\text{As}_{\text{Hg}}$ ,  $\text{Te}_{\text{Hg}}$ , and  $\text{V}_{\text{Hg}}$  indicate As atom residing on the Hg sublattice, Te antisite, and Hg vacancy.  $\text{As}_{\text{Hg}}$  and  $\text{V}_{\text{Hg}}$  are isolated donor and acceptor at high temperature, and are bounded together to form complex at extremely low temperatures.  $\text{V}_{\text{Hg}}^{\text{II}}$  suggests a possible second  $\text{V}_{\text{Hg}}$  acceptor level, question mark (?) indicates the possible origin of As tetramer  $[(\text{As}_{\text{Hg}}\text{-As}_i)_{\text{dimmer}}]_3$ . The values describe impurity levels relative to the band extrema. B3, B2, B1, DA, D2, and D1 represent the PR processes as depicted in Figs. 9 and 11.

The bandedge electronic structure can therefore be drawn as schematically shown in Fig. 13, together with the corresponding impurity-level energies for as-grown As-doped  $\text{HgCdTe}$  layers prepared by MBE technique. It is noteworthy that while the impurity levels are rather certain for  $\text{As}_{\text{Hg}}$ ,  $\text{Te}_{\text{Hg}}$ , and  $\text{V}_{\text{Hg}}$ , the value of 69 meV for  $\text{V}_{\text{Hg}}^{\text{II}}$  needs to be treated with care as it is at the moment a preliminary assumption, and a value of 39 meV may be also possible if it in fact relates to the D2 feature. The level indicated by question mark is likely due to As tetramer of  $[(\text{As}_{\text{Hg}}\text{-As}_i)_{\text{dimmer}}]_3$ , the value of which is 42 meV when it relates to the D2 feature, or 72 meV if it actually leads to the D1 feature.

With the aid of the assignment of the main PR features, it is now possible to make a brief discussion of the physical meaning of the empirical formula established by Hansen *et al.*, which has been widely used as a good approximation of cutoff energy for  $\text{Hg}_{1-x}\text{Cd}_x\text{Te}$  material's optoelectronic response. As illustrated in Fig. 10(a), the empirical formula roughly represents at different temperature the energy of the transition, of which the intensity/possibility is in general the strongest one at that temperature. Only at about room temperature is it close to the *real* band-gap energy of the material. Previously, it was shown that the main PR peak is energetically coincident to the cutoff of photocurrent spectrum quite well at 77 K.<sup>31</sup> It is therefore clear that the energy by Hansen *et al.*'s formula predicts an "equivalent" band gap, which is not only determined by the real band gap but also affected by the shallow impurities, and is slightly higher than but very close to the energy separation between the shallow donor and shallow acceptor levels in a temperature range of about 77 K where  $\text{HgCdTe}$  materials and devices are commonly applied. From optoelectronic response point of view, this means that the photoelectronic transition does not corresponds to band-to-band process at most of the temperature conditions particularly at 77 K. In contrast, the processes of

shallow donor-shallow acceptor and shallow impurity-band in HgCdTe may play a key role. It may hence provide a new perspective for the control of the cutoff energy of materials and devices, and a further support for the reliability of using PR as a noncontact experimental alternative in predicting the cutoff energy of narrow-gap HgCdTe.<sup>31</sup>

#### IV. SUMMARY

To summarize, temperature-dependent infrared PR study is carried out systematically on as-grown narrow-gap HgCdTe epilayers with different As-doping levels prepared by molecular-beam epitaxy, by using a step-scan FTIR spectrometer-based PR technique. Direct PR evidences as well as their evolution with temperature are observed for the band-gap, below-band-gap, and above-band-gap processes. Analyses indicate that for the as-grown As-doped samples with doping levels of about  $4 \times 10^{16} \text{ cm}^{-3}$  and  $3 \times 10^{17} \text{ cm}^{-3}$ , both the photomodulation-induced FPI effect and the FKO effect are significant on the low- and high-energy sides of the main PR features, respectively. For the sample with a significantly higher doping level of  $6 \times 10^{18} \text{ cm}^{-3}$ , however, neither the photomodulation-induced FPI nor the FKO is obvious, making deep-level related weak PR features well resolved. The PR features are fitted by derivative line shape function, except for the photomodulation-induced FPI and FKO ones, and the evolution of the critical energy with temperature is revealed. The mechanisms of particular PR features are inferred and the impurity levels are

estimated to be about  $17 \pm 1 \text{ meV}$  and  $27 \pm 3 \text{ meV}$  below the conduction-band minimum for  $\text{As}_{\text{Hg}}$  and  $\text{Te}_{\text{Hg}}$ , and  $14 \pm 1 \text{ meV}$  above the valence-band maximum for the first acceptor level of  $V_{\text{Hg}}$ , respectively. Evidences for both the second acceptor level of mercury vacancy ( $V_{\text{Hg}}^{\text{II}}$ ) and the possible As tetramer are detected. An energy of about 69 meV above the valence-band maximum is supposed preliminarily for the  $V_{\text{Hg}}^{\text{II}}$  acceptor level and 42 meV below the conduction-band minimum for the As tetramer  $[(\text{As}_{\text{Hg}}\text{-As}_i)_{\text{dimmer}}]_3$  at 77 K. The bandedge electronic structure is hence established for as-grown As-doped narrow-gap HgCdTe layers. A comparison of the temperature-dependent energies of the main PR features is made with the prediction of the band-gap energy by a widely used empirical formula, and the physical meaning of “effective band gap” is clarified for the empirical formula.

#### ACKNOWLEDGMENTS

One of the authors (J.S.) thanks Guoliang Shi for technical supports, Liangqing Zhu for the assistance in running the laboratory, and Tienan Zhao for the help around the  $\text{Ar}^+$  laser. The work was sponsored by the Science and Technology Commission of Shanghai Municipality (Grants No. 08XD14047 and No. 09JC1415600), the National Natural Science Foundation of China (Grants No. 60676063 and No. 60876012), and the National Basic Research Program of China (Grant No. 2007CB924902).

\*Author to whom correspondence should be addressed; jshao@mail.sitp.ac.cn

<sup>1</sup>G. L. Hansen, J. L. Schmidt, and T. N. Casselman, *J. Appl. Phys.* **53**, 7099 (1982).

<sup>2</sup>M. A. Berding, M. van Schilfgaarde, and A. Sher, *Phys. Rev. B* **50**, 1519 (1994).

<sup>3</sup>M. Zandian, A. C. Chen, D. D. Edwall, J. G. Pasko, and J. M. Arias, *Appl. Phys. Lett.* **71**, 2815 (1997).

<sup>4</sup>P. Boieriu, C. H. Grein, H. S. Jung, J. Garland, and V. Nathan, *Appl. Phys. Lett.* **86**, 212106 (2005).

<sup>5</sup>J. R. Lindle, W. W. Bewley, I. Vurgaftman, J. R. Meyer, M. L. Thomas, E. C. Piquette, D. D. Edwall, and W. E. Tennant, *Appl. Phys. Lett.* **90**, 241119 (2007).

<sup>6</sup>Y. Chang, C. H. Grein, J. Zhao, C. R. Becker, M. E. Flatte, P.-K. Liao, F. Aqariden, and S. Sivananthan, *Appl. Phys. Lett.* **93**, 192111 (2008).

<sup>7</sup>A. Rogalski, J. Antoszewski, and L. Faraone, *J. Appl. Phys.* **105**, 091101 (2009).

<sup>8</sup>B. Gelmont, K.-S. Kim, and M. Shur, *Phys. Rev. Lett.* **69**, 1280 (1992).

<sup>9</sup>F. Fuchs, H. Schneider, P. Koidl, K. Schwarz, H. Walcher, and R. Triboulet, *Phys. Rev. Lett.* **67**, 1310 (1991).

<sup>10</sup>W. Yang, K. Chang, and S.-C. Zhang, *Phys. Rev. Lett.* **100**, 056602 (2008).

<sup>11</sup>E. M. Sheregii, J. Cebulski, A. Marcelli, and M. Piccinini, *Phys. Rev. Lett.* **102**, 045504 (2009).

<sup>12</sup>J. H. Chu, S. Q. Xu, and D. Y. Tang, *Appl. Phys. Lett.* **43**, 1064 (1983).

<sup>13</sup>M. A. Berding and A. Sher, *Appl. Phys. Lett.* **74**, 685 (1999).

<sup>14</sup>L. Z. Sun, X. S. Chen, Y. L. Sun, X. H. Zhou, Z. J. Quan, H. Duan, and W. Lu, *Phys. Rev. B* **71**, 193203 (2005).

<sup>15</sup>X. H. Shi, S. Rujirawat, R. Ashokan, C. H. Grein, and S. Sivananthan, *Appl. Phys. Lett.* **73**, 638 (1998).

<sup>16</sup>Y. S. Ryu, Y. B. Heo, B. S. Song, S. J. Yoon, Y. J. Kim, and T. W. Kang, *Appl. Phys. Lett.* **83**, 3776 (2003).

<sup>17</sup>I. I. Izhnin, S. A. Dvoretzky, N. N. Mikhailov, Y. G. Sidorov, V. S. Varavin, and K. D. Mynbaev, *Appl. Phys. Lett.* **91**, 132106 (2007).

<sup>18</sup>F. Yue, J. Shao, X. Lü, J. Wu, W. Huang, X. Lin, L. He, and J. Chu, *Appl. Phys. Lett.* **89**, 021912 (2006).

<sup>19</sup>F. X. Zha, J. Shao, J. Jiang, and W. Y. Yang, *Appl. Phys. Lett.* **90**, 201112 (2007).

<sup>20</sup>F. G. Pollak and H. Shen, *Mater. Sci. Eng. R.* **10**, 275 (1993).

<sup>21</sup>G. Gumbs, D. Huang, H. Qiang, F. H. Pollak, P. D. Wang, C. M. Sotomayor Torres, and M. C. Holland, *Phys. Rev. B* **50**, 10962 (1994).

<sup>22</sup>Y. Mochizuki, T. Ishii, M. Mizuta, A. Mochizuki, and J. M. Langer, *Phys. Rev. Lett.* **77**, 3601 (1996).

<sup>23</sup>T. M. Hsu, W.-H. Chang, K. F. Tsai, J.-I. Chyi, N. T. Yeh, and T. E. Nee, *Phys. Rev. B* **60**, R2189 (1999).

<sup>24</sup>M. Muñoz, F. H. Pollak, M. B. Zakia, N. B. Patel, and J. L. Herrera-Pérez, *Phys. Rev. B* **62**, 16600 (2000).

- <sup>25</sup>A. Kaneta and S. Adachi, *J. Appl. Phys.* **87**, 7360 (2000).
- <sup>26</sup>A. Imada, S. Ozaki, and S. Adachi, *J. Appl. Phys.* **92**, 1793 (2002).
- <sup>27</sup>H. Shen, S. H. Pan, F. H. Pollak, and R. N. Sacks, *Phys. Rev. B* **37**, 10919 (1988).
- <sup>28</sup>J. Shao, R. Winterhoff, A. Dörnen, E. Baars, and J. Chu, *Phys. Rev. B* **68**, 165327 (2003).
- <sup>29</sup>J. Shao, F. Yue, X. Lü, W. Lu, W. Huang, Z. Li, S. Guo, and J. Chu, *Appl. Phys. Lett.* **89**, 182121 (2006).
- <sup>30</sup>J. Shao, W. Lu, F. Yue, X. Lü, W. Huang, Z. Li, S. Guo, and J. Chu, *Rev. Sci. Instrum.* **78**, 013111 (2007).
- <sup>31</sup>J. Shao, X. Lü, W. Lu, F. Yue, W. Huang, N. Li, J. Wu, L. He, and J. Chu, *Appl. Phys. Lett.* **90**, 171101 (2007).
- <sup>32</sup>J. Shao, L. Ma, X. Lü, W. Lu, J. Wu, F.-X. Zha, Y.-F. Wei, Z.-F. Li, S.-L. Guo, J.-R. Yang, L. He, and J.-H. Chu, *Appl. Phys. Lett.* **93**, 131914 (2008).
- <sup>33</sup>J. Shao, L. Chen, X. Lü, W. Lu, L. He, S. Guo, and J. Chu, *Appl. Phys. Lett.* **95**, 041908 (2009).
- <sup>34</sup>L. He, J. R. Yang, S. L. Wang, S. P. Guo, M. F. Yu, X. Q. Chen, W. Z. Fang, Y. M. Qiao, Q. Y. Zhang, R. J. Ding, and T. L. Xin, *J. Cryst. Growth* **175-176**, 677 (1997).
- <sup>35</sup>F. Aqariden, H. D. Shih, M. A. Kinch, and H. F. Schaake, *Appl. Phys. Lett.* **78**, 3481 (2001).
- <sup>36</sup>Y. Selamet, C. H. Grein, T. S. Lee, and S. Sivananthan, *J. Vac. Sci. Technol. B* **19**, 1488 (2001).
- <sup>37</sup>D. E. Aspnes, *Surf. Sci.* **37**, 418 (1973).
- <sup>38</sup>H. Shen and M. Dutta, *J. Appl. Phys.* **78**, 2151 (1995).
- <sup>39</sup>M. Sydor, J. Angelo, J. J. Wilson, W. C. Mitchel, and M. Y. Yen, *Phys. Rev. B* **40**, 8473 (1989).
- <sup>40</sup>F. Cerdeira, C. Vázquez-López, E. Ribeiro, P. A. M. Rodrigues, V. Lemos, M. A. Sacilotti, and A. P. Roth, *Phys. Rev. B* **42**, 9480 (1990).
- <sup>41</sup>D. Huang, D. Mui, and H. Morkoç, *J. Appl. Phys.* **66**, 358 (1989).
- <sup>42</sup>J. Shao, Ph.D. thesis, Universität Stuttgart, 2002.
- <sup>43</sup>H. Röppischer, N. Stein, U. Behn, and A. B. Novikov, *J. Appl. Phys.* **76**, 4340 (1994).
- <sup>44</sup>M. A. Berding, A. Sher, M. van Schilfgaarde, A. C. Chen, and J. Arias, *J. Electron. Mater.* **27**, 605 (1998).
- <sup>45</sup>L. He, X. Fu, Q. Wei, W. Wang, L. Chen, Y. Wu, X. Hu, J. Yang, Q. Zhang, R. Ding, X. Chen, and W. Lu, *J. Electron. Mater.* **37**, 1189 (2008).